Electrochimica Acta 330 (2020) 135275

Contents lists available at ScienceDirect

Electrochimica Acta

journal homepage: www.elsevier.com/locate/electacta

Discharging behavior of confined bipolar electrodes: Coupled electrokinetic and electrochemical dynamics

A. Eden [a, *], K. Scida [a], N. Arroyo-Currás [b], J.C.T. Eijkel [c, d], C.D. Meinhart [a], S. Pennathur [a]

[a] Department of Mechanical Engineering, University of California Santa Barbara, Santa Barbara, CA, 93101, United States
[b] Department of Pharmacology and Molecular Sciences, Johns Hopkins School of Medicine, Baltimore, MD, 21205, United States
[c] Technical Medical (TechMed) Centre, University of Twente, Enschede, the Netherlands
[d] BIOS Lab-on-a-Chip, MESA+ Institute for Nanotechnology, University of Twente, Enschede, the Netherlands

ARTICLE INFO

Article history:
Received 6 August 2019
Received in revised form
23 October 2019
Accepted 10 November 2019
Available online 13 November 2019

Keywords:
Bipolar electrochemistry
Electrical double layers
Induced-charge electrokinetics
Discharging dynamics
Nanofluidics

ABSTRACT

In this study we numerically investigate the intimately coupled transient electrokinetic and electrochemical dynamics of a nanoconfined bipolar electrode system, using experimental results to guide our analysis. Our recently developed 2D numerical model implements the Poisson-Nernst-Planck-Stokes system of equations to describe nanoscale chemical species transport by advection, migration, and diffusion, as well as the presence of both homogenous and heterogeneous reactions. By eschewing the assumption of electroneutrality and resolving diffuse-charge screening effects, our model uniquely accounts for a wide range of nonlinear transient effects including bipolar electrode (BPE) surface polarization, Faradaic charge accumulation, induced-charge electroosmotic flow, and ion concentration polarization. Using this model, we demonstrate that upon the removal of a polarizing electric field, excess accumulated charge at a BPE surface electrochemically discharges following the capacitive relaxation of diffuse space charge in the electrical double layers (EDLs) surrounding the BPE extremities. These EDLs continue to polarize the BPE as they relax by a process of drift-diffusion, wherein the counter-ionic space charge at each pole promotes a large influx of oppositely charged ions to restore electroneutrality. We numerically reproduced this electrokinetic enhancement effect that was first observed in a recently reported experimental system in which charged fluorophores were used as tracer molecules. Our results also support experimental evidence that, following capacitive EDL relaxation, nanoconfined BPEs can exhibit pseudocapacitance-like discharging behavior that is localized to a single end of the electrode; we experimentally linked this localization to surface oxidation of the anodic BPE pole under the applied field. In addition to providing important insight into the interplay between nanoscale electrokinetic and electrochemical phenomena that govern transient electrode processes, our model and the results presented in this work reinforce the notion that the domain of bipolar electrochemistry constitutes a promising frontier for developing “wirelessly” tunable charge storage and visual detection approaches which exploit both electrokinetic and Faradaic mechanisms.

1. Introduction

Understanding the transient dynamics of electrochemical cells is of paramount importance for the development of modern energy conversion and storage technologies such as rechargeable batteries [1], fuel cells [2,3], redox flow cells [4] and supercapacitors [5,6]. Knowledge of electrochemical transients is also fundamental for the correct interpretation of electroanalytical measurements utilizing techniques ranging from well-established voltammetry [7,8] and electrochemical impedance spectroscopy methods [9,10] to nascent hybrid approaches [11,12]. Thus, a strong foundational understanding of the relevant charge transfer and mass transport processes is necessary to guide development of next-generation devices, which are increasingly being sought in the form of miniaturized, electronically integrated energy systems [13,14] and on-chip electroanalytical platforms [15–17].

The confinement of electrochemical systems to micro- and nanoscale dimensions imparts a multitude of benefits, including

* Corresponding author.
E-mail addresses: a_eden@ucsb.edu (A. Eden), kscida@ucsb.edu (K. Scida), netzarroyo@jhmi.edu (N. Arroyo-Currás), j.c.t.eijkel@utwente.nl (J.C.T. Eijkel), meinhart@ucsb.edu (C.D. Meinhart), sumita@ucsb.edu (S. Pennathur).

https://doi.org/10.1016/j.electacta.2019.135275
0013-4686/

improved reaction rates and faster response times due to shorter mass transport time scales [18]. Moreover, micro-to-nanoscale confinement significantly enhances analyte-surface interactions and enables the engineering of high surface capacitances which dramatically improve electrical double layer capacitor technologies [6,19]. Finally, confined systems are particularly advantageous in analytical applications because they require smaller sample volumes and are highly amenable to process parallelization [20]. However, the benefits of geometric confinement come at the cost of increased physical complexity of such systems due, in large part, to the increased importance of electric double layer structures within miniaturized architectures. Frumkin [21], in particular, was instrumental in elucidating the influence of electrostatically polarized surfaces on reactant concentrations and driving potentials in dilute-solution electrochemical kinetics. Extensive pioneering efforts [18,22–28] have since been undertaken to harness the power of modern computational capabilities in order to incorporate these microscopic effects and extend our understanding of nanoscale processes beyond conventional theoretical analyses. Many of these numerical studies rely on simplified canonical geometries or limiting cases, however, and thus tend to lag behind experimental innovation and expansion into domains which exploit exotic phenomena. This is especially true for modern microfabricated devices, which increasingly employ customized and often heterogeneous architectures to realize novel analytical platforms [15–17,29].

One on-chip process that has recently gained renewed attention is bipolar electrochemistry, a "wireless" technique which leverages electric-field-induced polarization of isolated conductors immersed in solution to drive coupled oxidation and reduction reactions at spatially distinct poles [30,31]. Exploiting this bipolar effect has shown promise in developing analytical platforms for analyte separation [32,33] and detection [15,16], as well as the synthesis of micro/nanostructures [34] and characterization of electrocatalysts [35,36], to name a few. Such applications often involve complex reaction mechanisms and coupled transport processes, however, and our current understanding of transient BPE dynamics at the nanoscale remains limited because contemporary numerical models [15,37–40] often fail to fully describe their behavior under confinement. These shortcomings stem from a range of assumptions and oversimplifications made with respect to EDLs and electroneutrality, nonlinear induced-charge electroosmotic flow (ICEOF), homogeneous buffer reactions, and/or mass-transfer limitations on heterogeneous reaction kinetics. Each of these effects can play an important role in the charging and discharging characteristics of confined electrodes – both conventional and bipolar – as well as the accompanying electrokinetic phenomena occurring in adjacent electrolyte solutions [37,41].

We have recently introduced in the literature [42] a comprehensive 2D numerical model of nanoscale bipolar electrochemistry in which we simultaneously include the coupled effects of 1) nonlinear BPE surface capacitance, 2) Faradaic reactions and charge accumulation, 3) ionic migration and diffuse-charge screening, 4) homogeneous buffer reactions, and 5) advective transport by electroosmotic flow (EOF) and ICEOF. In the present study, we apply this model to probe the transient behavior of a nanochannel-confined BPE system after a polarizing electric field is rapidly removed. Our analysis provides a stark contrast to the vast majority of published reports which limit their scope to examining quasi-steady conditions achieved under an applied field. We also briefly investigate the influence of a resistive oxide thin film formed at the anodic BPE pole on the system dynamics. Our findings reveal a close interplay between EDL relaxation, Faradaic discharge, and mass transport in the confined system across disparate time scales. The results are supported by qualitative comparison with experimental observations of charged, pH-sensitive fluorophores which indirectly reveal effects of both electrochemical reactions and nanoscale electrokinetic interactions [41]. On this basis, we raise the possibility of applying wireless bipolar electrochemistry to develop capacitive and Faradaic discharge detection methods.

2. Experimental methods

A detailed description of the experimental components and procedures can be found in Ref. [41]. Briefly, we fabricated arrays of fused silica nanofluidic channels 300–600 nm tall, 500 μm wide, and 1 cm long via reactive ion etching. Floating Pt electrodes 80 nm thick with a 20 nm Ti adhesion layer were deposited in the channels, and the resulting structures were bonded to a separate fused silica wafer containing fluidic reservoir ports. Following serial cleaning of the channels with 0.1 M NaOH and deionized water, fluorescence experiments were carried out with a mixture of 100 μM sodium fluorescein and 1.0 mM sodium phosphate buffer at pH 7.5. Platinum driving electrodes were inserted into the reservoirs and an external power supply was used to introduce, maintain, and then remove a potential difference (30 V or 250 V) between the electrodes after 30 s. Images were captured at 3.3 Hz and processed using ImageJ v2 1.52e and custom Python v3.6.3 scripts.

3. Theory

Our model, summarized here, considers a system consisting of two electrolyte reservoirs connected by a nanochannel (Fig. 1a). An electronically isolated platinum electrode situated in the center of the channel acts as a floating BPE when an electric field is generated between two driving electrodes located in the reservoirs (Fig. 1b). The applied field drives electron redistribution at the equipotential electrode surface, resulting in charge segregation and the subsequent formation of a negatively charged cathodic pole and a positively charged anodic pole at the electrode extremities (Fig. 1c) [30]. EDLs form in solution to screen the charge arising from BPE polarization, introducing electrostatic interactions which affect the kinetics of redox reactions occurring at the poles [21] and also give rise to strongly coupled electrokinetic transport phenomena such as induced-charge electroosmotic flow [42,43] and ion concentration polarization (CP) [37,44–46].

We numerically represented the experimental system by modeling a 2D cross-sectional plane through the center of the channel and reservoirs (Fig. 1b) using commercial finite-element software (COMSOL Multiphysics v5.4). The BPE-width-to-channel-height aspect ratio (333:1 for a 300 nm tall channel) is sufficiently large to assume no significant variation in transport conditions upon translation of the cross-sectional plane by a small amount in the y-direction; hence, a 2D model is suitable for our analysis. Because of the intensive computational demands of nanoscale electrokinetic transport equations which include charge screening effects on spatially nonuniform electrochemical dynamics, our numerical efforts are limited to simulating a substantially shorter system length than the experimental analogue (in this study we simulate a 5 μm long channel with a 1.5 μm long BPE, as compared with the 1 cm long experimental system which contains a 500 μm long BPE). This leads to a natural discrepancy between the longitudinal time scales of the various physicochemical processes involved in our system; these discrepancies are compounded by fundamental limitations such as electronic equipment response times which further obviate direct quantitative comparisons of dynamical behavior between simulation and experiment. As a result, we aim to recreate experimental observations merely on a qualitative basis, though our model nevertheless yields results that

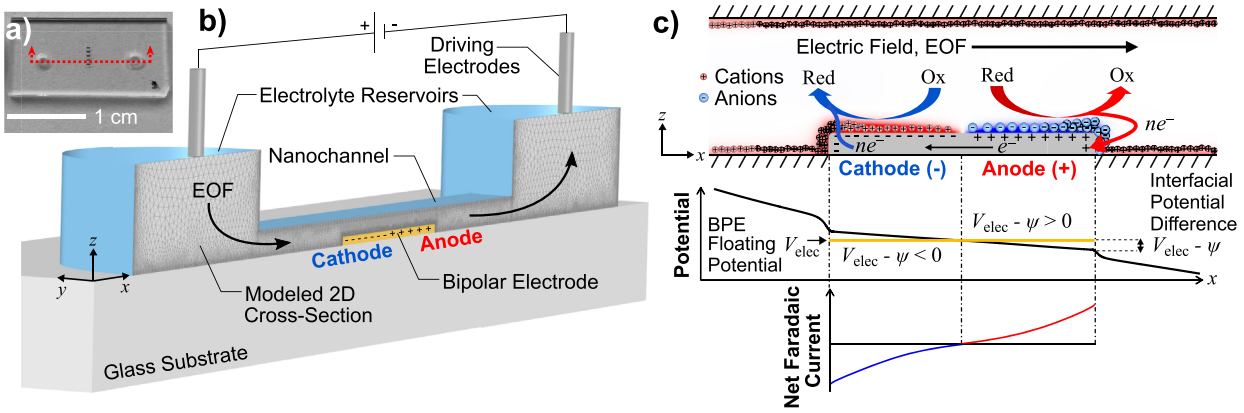

Fig. 1. The nanochannel-confined bipolar electrochemical system represented in our model: (a) photograph of a fabricated nanofluidic array containing BPEs (dark bands at the center of the image), (b) schematic cross-section of a single-channel device showing the modeled 2D plane (diagram not to scale), and (c) schematic depicting characteristic ionic charge distribution, interfacial potential difference, and Faradaic reactions at the confined BPE. Part (c) was adapted with permission from Ref. [42] (Eden et al., Modeling Faradaic reactions and electrokinetic phenomena at a nanochannel-confined bipolar electrode. *J. Phys. Chem. C* **2019**, *123*, 5353−5364). Copyright 2019 American Chemical Society.

are consistent with the observed experimental phenomena and provide key physical insights into the intrinsically interconnected processes accompanying BPE discharge.

Our model considers the hydrogen evolution and oxidation reactions (HER and HOR, respectively), as well as the oxygen evolution and reduction reactions (OER and ORR), which occur at the BPE/electrolyte interface. We also include the acid-base chemistry of the dilute supporting electrolyte (1.0 mM sodium phosphate at pH 7.5) and the presence of a pH-sensitive fluorophore (0.1 mM of sodium fluorescein, referred to hereafter as FL or FL^{2-}) used for experimental visualization. Additionally, we assume that H_2O is present in excess quantities, such that the only mass-transfer limitations in the considered reactions arise from the transport of H^+, OH^-, H_2, and O_2 to and from the BPE surface [47]. In acidic and alkaline media, respectively, the reversible HER/HOR final balance reactions are given by

$$2H^+ + 2e^- \rightleftarrows H_2, \tag{1}$$

$$2H_2O + 2e^- \rightleftarrows H_2 + 2OH^-. \tag{2}$$

The acidic and alkaline OER/ORR final balance reactions are, respectively, given by

$$4H^+ + O_2 + 4e^- \rightleftarrows 2H_2O, \tag{3}$$

$$2H_2O + O_2 + 4e^- \rightleftarrows 4OH^-. \tag{4}$$

Although the starting pH of the system (7.5) is nearly neutral, sharp and dynamic pH gradients will form and propagate some distance through the channel [31,41,48] due to (1) concomitantly produced and consumed H^+ and OH^- ions at the respective BPE poles, (2) the weak buffering capacity of the dilute supporting electrolyte, and (3) the limited volume of electrolyte available within the nanoconfined channel. As a consequence, we expect that the reactions at the cathodic pole (H^+ consumed, OH^- produced) will eventually be dominated by equations (2) and (4), while equations (1) and (3) will eventually become the dominant anodic pole (H^+ produced, OH^- consumed) reactions (see Ref. [42] for more details).

The transport of each of the ten chemical species present in our system (H^+, OH^-, H_2, O_2, Na^+, H_3PO_4, $H_2PO_4^-$, HPO_4^{2-}, PO_4^{3-}, FL^{2-}), is governed by a statement of mass conservation with Nernst-Planck fluxes [49],

$$\frac{\partial c_i}{\partial t} = -\nabla \cdot \left(\mathbf{u}c_i - D_i \nabla c_i - \frac{D_i}{RT} z_i F c_i \nabla \psi \right) + R_i, \tag{5}$$

in which c_i is the concentration of species i, $\mathbf{u}$ is the fluid velocity vector, D_i is the diffusion coefficient, z_i is the valence, R is the ideal gas constant, T is the solution temperature (assumed to be 25° Celsius), F is Faraday's constant, ψ is the electrostatic potential in solution, and R_i is the homogeneous reaction source term (only applicable for H^+, OH^-, H_3PO_4, $H_2PO_4^-$, HPO_4^{2-}, and PO_4^{3-}). We include reaction source terms for the association/dissociation reactions of water, as well as the triprotic phosphate buffer system that comprises our supporting electrolyte. At the top surface of each reservoir, we specify Dirichlet boundary conditions to fix the local concentration of each species at the respective bulk concentrations calculated by the bulk pH, equilibrium statements, and electroneutrality (see the Supplementary Material). We enforce zero normal flux conditions for all species at the channel and reservoir walls, as well as at the BPE surface for species Na^+, H_3PO_4, $H_2PO_4^-$, HPO_4^{2-}, PO_4^{3-} and FL^{2-}. The normal fluxes of participating redox-active species at the BPE surface (H^+, OH^-, H_2, O_2) are individually specified via Faraday's laws of elecrolysis using the corresponding reaction current densities [50].

In addition to the charge present at the polarized BPE surface, we assume that the channel walls maintain a negative native surface charge due to the protonation/deprotonation of surface-bound silanol groups [51]. To account for the applied electric field in the bulk solution, as well as ionic charge screening within the resulting channel wall and BPE EDLs, we calculate the mean-field electrostatic potential ψ using Poisson's equation,

$$-\nabla \cdot (\varepsilon \nabla \psi) = \sum_{i=1}^{n} F z_i c_i, \tag{6}$$

where ε is the solvent permittivity and n is the total number of species in solution. The permittivity of water is known to be a function of the local electric field at high field strengths [52], as the degree of solvent molecule polarizability is reduced when the molecules are already strongly oriented. We incorporated this effect in our model, which occurs primarily within EDLs surrounding highly charged surfaces, by implementing a local field-dependent permittivity as defined by Booth [19,52].

To resolve the extremely fast dynamics that can occur in our nanoscale system, we apply a Dirichlet boundary condition at the

top surface of the inlet (left) reservoir that specifies the electric potential as a smoothed time-dependent step function which transitions from zero to an applied potential (or vice versa for discharging) over a time interval of 5 ns (see Supplementary Material Fig. S1). The electric potential at the top surface of the outlet (right) reservoir is fixed to zero at all times. At the reservoir and channel walls, a Neumann condition prescribes the normal component of the displacement field to be equal to a predefined wall surface charge; in reality, this native charge is a function of the local solution pH and ionic strength [47,51], though we adopt the common numerical assumption of a fixed wall charge in the present study (future efforts which incorporate these local surface chemistry effects will likely yield additional interesting phenomena, particularly at large applied potentials). At the BPE, the surface charge is a function of the local electrode/electrolyte interfacial potential difference. Assuming no specific adsorption of charged species, the Stern layer potential drop in the common Gouy-Chapman-Stern EDL model is linear [18,53] and the BPE interfacial charge is given by the Robin condition

$$\sigma_{\mathrm{BPE}} = \mathbf{n}\cdot\nabla(\varepsilon\psi) = C_{\mathrm{S}}(V_{\mathrm{elec}} - \psi)|_{\mathrm{S}}, \tag{7}$$

where V_{elec} is the floating electrode potential, $\mathbf{n}$ is the outward unit normal vector, and C_{S} is an effective Stern layer capacitance. As the Stern layer is assumed to consist solely of polarized solvent molecules, it can be approximated as a capacitive element of capacitance $C_S = \varepsilon/\lambda_S$ with a locally defined permittivity and a hypothetical fixed width λ_S that is on the order of a hydrated ionic radius [24].

Interactions between diffuse ionic charge and the lateral component of the applied electric field introduce Coulombic forces within the channel wall and BPE EDLs which drive bulk fluid motion by viscous shear [50]. Oppositely charged EDLs at the BPE poles experience opposing electrical forces which drive ICEOF-generated hydrodynamic recirculation above the BPE [43]. Thus, the advective species transport term from equation (5) and the electrostatic field from equation (6) are inherently coupled to conservation of mass and momentum for the fluid flow via Stokes' equation and continuity for an incompressible Newtonian fluid,

$$\rho\frac{\partial\mathbf{u}}{\partial t} = \eta\nabla^2\mathbf{u} - \nabla p - \sum_{i=1}^{n} Fz_i c_i \nabla\psi; \nabla\cdot\mathbf{u} = 0, \tag{8}$$

where ρ is the mass density of the fluid, η is the dynamic viscosity of the fluid, and p is the local fluid pressure.

Following Frumkin's theoretical discoveries [21] and more recent numerical models by Bazant and coworkers [18,22–27], we assume that Faradaic reactions occur at a fixed reaction plane of closest approach located at the Stern/diffuse layer interface; thus, the electrostatic energy which drives interfacial charge transfer reactions stems from the potential drop across the Stern layer $\Delta V_{\mathrm{S}} = (V_{\mathrm{elec}} - \psi)|_{\mathrm{S}}$ rather than the entire metal-to-bulk-solution potential difference [47]. For a BPE configuration, the surface concentrations of charged reactant species H^+ and OH^- at the reaction plane vary spatially along the electrode surface due to the nonuniform interfacial potential and charge distributions [30,42]. To describe the local Faradaic current density for each reaction, we implement the generalized Frumkin-Butler-Volmer (gFBV) equation directly at the Stern/diffuse layer interface of the BPE EDLs [25],

$$j_{\mathrm{F},r} = K_{\mathrm{a},r}c_{\mathrm{red},r}\exp\left(\frac{\alpha_{\mathrm{a},r}n_rF\Delta V_{\mathrm{S}}}{RT}\right) - K_{\mathrm{c},r}c_{\mathrm{ox},r}\exp\left(-\frac{\alpha_{c,r}n_rF\Delta V_{\mathrm{S}}}{RT}\right), \tag{9}$$

where $j_{\mathrm{F},r}$ is the local Faradaic reaction current density for reaction r, $c_{\mathrm{ox},r}$ and $c_{\mathrm{red},r}$ are the mathematical products of oxidized and reduced species concentrations at the reaction plane for reaction r (assuming electrochemical reaction orders of 1 [18,47]), $K_{\mathrm{c},r}$ is the cathodic rate constant, $\alpha_{\mathrm{c},r}$ is the cathodic charge transfer coefficient, n_r is the number of electrons transferred per reaction, $K_{\mathrm{a},r}$ is the anodic rate constant, and $\alpha_{\mathrm{a},r}$ is the anodic charge transfer coefficient. By taking the interfacial potential relative to an equilibrium state with Stern layer potential difference $\Delta V_{\mathrm{S,eq}}$, we can conveniently express equation (9) using an exchange current density $j_{0,r}$ [25],

$$j_{\mathrm{F},r} = j_{0,r}\left[\frac{c_{\mathrm{red},r}}{c_{\mathrm{red,eq},r}}\exp\left(\frac{\alpha_{\mathrm{a},r}n_rF(\Delta V_{\mathrm{S}} - \Delta V_{\mathrm{S,eq},r})}{RT}\right) - \frac{c_{\mathrm{ox},r}}{c_{\mathrm{ox,eq},r}}\exp\left(-\frac{\alpha_{c,r}n_rF(\Delta V_{\mathrm{S}} - \Delta V_{\mathrm{S,eq},r})}{RT}\right)\right]. \tag{10}$$

Because the true equilibrium Stern layer potential difference is a complicated function of interdependent factors such as the electrochemical reaction kinetics, coupled charge screening effects, equilibrium concentrations of all participating redox species at the reaction plane, and the presence of dipoles or additional charged species at the surface [47], we assume a value of zero for simplicity in our qualitative system model.

The floating BPE potential is determined by a statement of global charge conservation. That is, at long times the equipotential BPE will float to the precise potential necessary in order to balance the current entering through the cathodic pole with the current exiting through the anodic pole, thereby preventing infinite charge accumulation. Faradaic charge accumulation *can* occur over some transient interval, however, if the cathodic and anodic currents are initially unbalanced, as is the case with charging Galvanic cells [50] and hybrid supercapacitors [5,6]. In Galvanic cells, for example, an analogous net charge is acquired by an electrode to impede the faster half-reaction and facilitate the slower half-reaction as the interface tends towards equilibrium. Any such Faradaic current imbalance in our BPE system is accounted for by a net capacitive displacement current which reflects the storage of charge at the surface and biases the interfacial charge/potential and EDLs towards a "charge-dominant" pole. Since these contributions are nonuniform over the BPE surface, we integrate the net Faradaic and displacement currents over the entire surface to enforce charge conservation and solve for V_{elec}. The net Faradaic current is obtained by summation over the total number of reactions m, $j_{\mathrm{F,net}} = \sum_{r=1}^{m} j_{\mathrm{F},r}$, while the displacement current is defined as the time derivative of the surface charge density. Thus, the total surface current is expressed as $j_{\mathrm{tot}} = j_{\mathrm{F,net}} + \frac{\partial}{\partial t}\left[C_{\mathrm{S}}(V_{\mathrm{elec}} - \psi)|_{\mathrm{S}}\right]$, and charge conservation subsequently requires that

$$\int_{\partial\Omega} j_{\mathrm{tot}} dS = 0. \tag{11}$$

The highly coupled equations which comprise this nanoscale model provide the most complete description to date of confined BPE dynamics [42], and offer unique insight into distinct transient processes occurring across as many as five spatial and ten temporal orders of magnitude in the present work.

4. Results and discussion

4.1. BPE transient dynamics

In general, four processes characterize the transient response of

a bipolar electrode subjected to an abrupt change in driving potential: (1) initial polarization/depolarization, (2) capacitive EDL formation/relaxation, (3) the onset/decay of Faradaic reactions, and (4) mass transport of reacting species [24,43,54]. In prior work [42], we discussed in detail the charging dynamics of nanoconfined BPEs upon the introduction of an external electric field. By contrast, here we focus mainly on the simulated dynamics of the system as it returns to equilibrium following the removal of the applied field.

The discharging dynamics of nanoconfined BPEs depend strongly on the history and duration of any prior electrical perturbations applied to the system, so we begin by briefly summarizing the state of our system after an external field has been applied. Upon the introduction of a potential difference across the nanochannel, solvent polarization establishes an electrostatic potential and associated electric field on the order of picoseconds [55]. The high mobility of electrons in the BPE allows the rapid redistribution of charge at the fluid/solid interface to establish an equipotential surface in response to the applied field, spatially segregating the isolated electrode into poles of positive and negative surface charge [30,31]. Ions in the adjacent electrolyte electrostatically interact with these oppositely charged poles and accordingly reorient to form EDLs which screen the interfacial charge. The fastest time scale associated with EDL formation is the Debye time, $\tau_D = \lambda_D^2/D$ (see Table 1), where λ_D is the Debye screening length and D is a characteristic diffusion coefficient, followed by the longer mixed (Ohmic) charging time, $\tau_O = R_{bulk}C_{EDL}$, where R_{bulk} is the electrical resistance of the electrolyte and C_{EDL} is the equivalent capacitance of the Stern and diffuse layers [23,43,54]. As diffuse charge accumulates during this capacitive process, the tangential component of the electric field subsequently begins to drive nonlinear ICEOF within the BPE EDLs. The native surface charge density at the fused silica walls also produces background EOF throughout the channel; these EDLs are already formed at equilibrium, however, and this directional EOF therefore initially develops independently of the BPE EDLs on the viscous time scale $\tau_v = H^2/\nu$, where ν is the kinematic viscosity of the solution [43].

If a sufficiently high interfacial potential difference develops across the compact Stern layer, electrochemical reactions proceed in parallel with EDL formation at the BPE surface. The time scale for BPE charging by heterogeneous charge transfer can similarly be expressed by an RC time constant, $\tau_{ct} = R_{ct}C_{EDL,}$ where R_{ct} is the interfacial charge transfer resistance and C_{EDL} is the equivalent capacitance of the compact and diffuse layers [47,54]. As with a Galvanic cell, any asymmetry in the net anodic and cathodic charge transfer rates results in unbalanced electron fluxes, leading to accumulation of charge at the metal/electrolyte interface and a compensatory shift in the electrode potential to balance the reaction rates [42]. If the electrochemical production or consumption rate of a given species exceeds the rate of mass transport to or from the surface, accumulation or depletion effects will propagate throughout the system and introduce a mass-transport dominated response on the order of the diffusion time scale $\tau_{diff} = L^2/D$ [23,24].

The state of the BPE after the initial transient charging period can be broadly classified into three categories: (1) an anodic case in which **a positive surface-integrated charge** (i.e., the net Faradaic current integrated over time and space) has accumulated at the BPE, (2) a cathodic case in which **a negative surface-integrated charge** has accumulated at the BPE, or (3) a neutral case with **negligible net charge** accumulation. In all three cases, the BPE poles are ultimately surrounded by charged EDLs which maintain a (zeta) potential difference between the Stern/diffuse layer interface and the bulk solution [36,43]. Recall Gauss's Law, which dictates that in regions of nonzero space charge density, the local electrostatic field changes in response to the space charge. Thus, if the applied field is removed faster than the diffuse space charge can possibly respond (i.e., the Debye time), then the same effective zeta potential and EDL ion distributions as present in the charged state persist shortly after the field removal. This is important because it follows that the metal/electrolyte potential difference at the BPE extremities also remains unchanged at the respective Stern layers; since it is this interfacial potential which drives heterogeneous charge transfer [18,47], Faradaic reactions briefly continue to occur at the same effective rate despite the absence of an applied potential difference across the channel.

The reactions thus continue unabated well beyond the Debye time (~10 ns), in which only initial EDL relaxation occurs. It is not until the Ohmic time scale (~10 μs) that we observe appreciable drift-diffusion of ions in the EDL and a subsequent reduction in both the surface charge distribution and Faradaic currents. The BPE remains polarized (i.e., bipolar) and opposing redox reactions continue at the respective poles as long as nonzero ionic space charge in the EDLs remains. Therefore, the BPE cannot fully discharge during this EDL relaxation period due to the similar rates of ongoing charge transfer at the two poles. Moreover, this delayed Faradaic discharge is also influenced by mass transport effects as concentration gradients formed near the BPE under the applied field continue to dissipate well into the longer diffusion time scale; these gradients can introduce variations in current due to concentration overpotentials [56].

The electrochemical accumulation of charge causes an interfacial potential bias towards one BPE pole [30] (Fig. 2), an effect which can arise due to asymmetries in the reaction rate constants, charge transfer coefficients, number of electrons transferred per reaction, and/or mass transfer conditions at the distinct poles. To reproduce

Table 1
Relevant time scales and characteristic values for the modeled BPE system [42].

Parameter	Equation	Characteristic Value
Debye time	$\tau_D = \lambda_D^2/D$	10 ns
Ohmic relaxation	$\tau_O = R_{bulk}C_{EDL}$	10 μs
Viscous time scale	$\tau_v = H^2/\nu$	90 ns
Charge transfer relaxation	$\tau_{ct} = R_{ct}C_{EDL}$	20 μs
Diffusion time	$\tau_{diff} = L^2/D$	650 μs
Geometric length scale	$L = L_{channel}/2$	2.5 μm
Bulk conductivity	$\kappa = F^2 \sum_{i=1}^{n} D_i z_i^2 c_{i,\infty}/RT$	0.15 mS/cm
Bulk resistance	$R_{bulk} = L/\kappa$	1.7 Ω cm^2
EDL capacitance	$C_{EDL} = \varepsilon\,(\lambda_D + \lambda_S)^{-1}$	70 mF/m^2
Debye length	$\lambda_D = \sqrt{\varepsilon RT\,(F^2 \sum_{i=1}^{n} a_i z_i^2)^{-1}}$ [a]	10 nm
Charge transfer resistance	$R_{ct} = RT/j_0F$	2.6 Ω cm^2

[a] a_i is the activity coefficient of species i in the bulk solution.

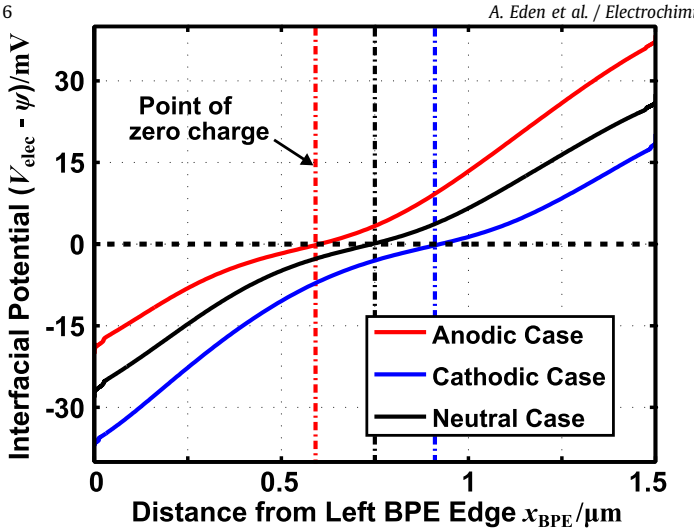

Fig. 2. Simulated interfacial potential distributions along the BPE surface for three different states at the end of charging: an anodic, cathodic, and neutral BPE. The applied potentials for these three cases were 1.6 V, 1.85 V, and 1.8 V, respectively (see the Supplementary Material for the different electrochemical kinetics parameters).

this effect, we numerically simulated artificial asymmetries by changing the rate of water oxidation relative to the other electrochemical reactions occurring in the system (see the Supplementary Material for parameter values for the different cases). For example, increasing the water oxidation rate facilitates charge transfer at the anodic pole, requiring a lower anodic interfacial potential magnitude relative to that of the cathodic pole (i.e., a cathodic case) in order to balance the net Faradaic current entering and leaving the electrode. As a consequence, the interfacial potential at the cathodic pole shifts to more negative values, indicating an excess of accumulated electrons at the electrode surface (blue trace in Fig. 2). Conversely, when the relative charge transfer rate at the anodic pole is reduced and more electrons initially leave the cathodic pole than enter the anodic pole (i.e., an anodic case), the interfacial potential magnitude at the anodic pole increases to compensate (red trace in Fig. 2) [30,42].

The diffuse-charge dynamics accompanying BPE charging and discharging are elucidated by examining the spatiotemporal evolution of the electric field lines (Fig. 3). Specifically, Fig. 3a and b depict capacitive EDL formation between the Debye and Ohmic times, while Fig. 3c demonstrates continuous flow of ionic current through the channel once the EDLs are mostly formed (Ohmic time) and Faradaic reactions begin to develop at the poles. As the BPE reaches its charged state (Fig. 3d), the space charge density profile reflects the cathodic-biased interfacial potential distribution from Fig. 2. Moreover, we observe an extended space charge layer near the cathodic pole at longer times, a result of ion concentration polarization that develops on the diffusion time scale. This nonlinear CP effect arises due to the competition between nonuniform advection and migration velocities of anions in different regions of the channel; partial short-circuiting of the nanochannel current by the BPE at large applied potentials [32,37] leads to a nonuniform electric field which reduces the relative importance of upstream anion migration (right to left) compared to advection (left to right) above the BPE, allowing EOF to locally dominate transport and drive anions away from the cathodic pole. Subsequent ion depletion from this region forms a layer of positive induced space charge slightly upstream of the cathodic pole (Fig. 3d) [37]. These effects locally extend the effective thickness of the cathodic EDL and introduce additional nonlinear electrokinetic phenomena such as EOF of the 2nd kind [57] in the nanochannel.

The field lines also reveal important system dynamics that continue after the applied potential is removed. Fig. 3e shows the system 100 ns after the driving field is removed, illustrating the early stages of capacitive EDL discharge. Note that this EDL relaxation is accompanied by a reversal in the electric field both upstream and downstream of the BPE (Fig. 3e and f). This behavior arises from an electrostatic potential difference between the BPE poles and the respective reservoirs. That is, the potential in the left and right reservoirs is effectively zero after the rapid removal of the applied potential, but there still remains a positive electrostatic potential associated with the cathodic EDL space charge and a negative potential associated with the anodic EDL space charge above the respective BPE poles. Thus, a positive potential gradient (i.e., negative axial electric field) is established upstream and downstream of the BPE, while a negative potential gradient (i.e., positive axial electric field) is briefly maintained in the region above the BPE as the EDLs relax by drift-diffusion. Due to the presence of this residual electric field, the decay time of EOF in the channel is also governed by BPE EDL relaxation. Finally, the transition from polarized BPE to Faradaically discharging cathode is clearly evidenced by the recession of the negative anodic EDL space charge in Fig. 3f, which ultimately leads to the uniform positive space charge above the discharging cathode in Fig. 3g.

During the drift-diffusion EDL relaxation process, the strong residual electric fields associated with the bipolar EDL space charge imbalances induce ionic migration for a short time in order to restore electroneutrality. Diffusion also aids in forcing these ions from the bulk towards the surface due to the large concentration gradients established by electrostatically depleted co-ions in the EDLs. Thus, the cation-rich EDL above the cathode will experience a large influx of anions on the order of the Ohmic time scale as the EDLs dissipate. This process can be visualized through fluorescence measurements of FL dye [41], and is demonstrated experimentally and numerically in Fig. 4. Note that although the charge of FL ions is pH-sensitive, we assume that all such ions near the cathode remain dianionic due to the high local pH [41,48]. It should also be noted that the time scales between our numerical simulation and experimental system differ by a factor of 10^5 due to disparities in experimental vs. modeled length scales (1 cm vs. 5 μm), as well as practical limitations on how quickly the applied potential can be experimentally removed by the power supply. Specifically, it was experimentally observed that the fluorescence intensity (caused by FL^{2-} ions) above the cathode transitioned over the course of approximately 0.5 s from relatively low (electrostatic repulsion) to relatively high (electrokinetic enhancement) as an influx of anions, including FL^{2-} ions, counteracted the remaining positive space charge. This nanoscale phenomenon, which was also previously demonstrated for anionic BODIPY fluorophores [41], raises the possibility of electrokinetic detection of specifically-tagged biomolecules in nanofluidic architectures by tracking a fluorescence signal during capacitive EDL discharge; in the present study, we experimentally observed the fluorescence intensity increase by up to a factor of 10.7 after the driving potential was removed (see Supplementary Material Fig. S2). This enhancement can be increased further by reducing the nanochannel height (thereby increasing the depth-averaged EDL fluorescence intensity) and employing a lower ionic strength electrolyte solution to increase the zeta potential [41].

Our calculations predict that the simulated bipolar EDLs fully relax and the BPE loses its polarization on the order of 10 μs (Ohmic time), around which time the positive/negative charge present at the pole of lower charge (i.e., the anodic pole for the cathodic case and the cathodic pole for the anodic case) vanishes. To demonstrate this effect, we separately calculated surface integrals of the positive and negative regions of the interfacial charge distribution over time

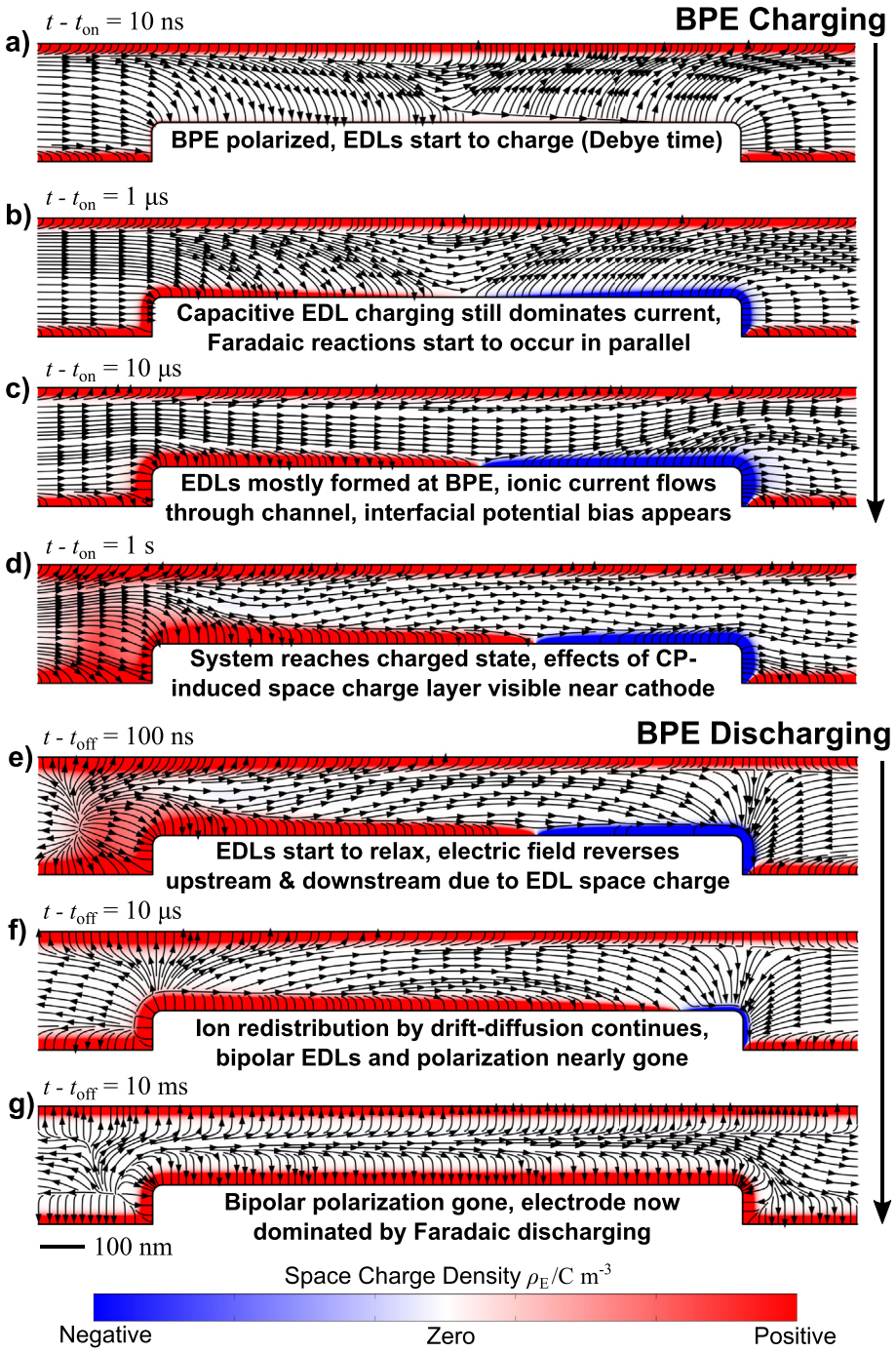

Fig. 3. Spatiotemporal evolution of the electric field lines and space charge density near the BPE during the charging and discharging processes for a cathodic case. Note that the color plots have artificial "contrast" added; the plotted range is truncated to $\pm 2.0 \times 10^4$ C/m^3 in order to simultaneously depict positive and negative space charge that can vary by orders of magnitude between EDLs at the channel walls and strongly polarized BPE. (For interpretation of the references to color in this figure legend, the reader is referred to the Web version of this article.)

and found that the surface charge distribution, and hence the interfacial potential distribution, attained a single polarity around this time (Figs. 3f and 5). Thus, changes in the local surface charge prior to this moment are primarily driven by dissipation of the bipolar EDLs above the electrode, while changes thereafter can be attributed to concentration overpotential and conventional Galvanic discharge of electrochemically accumulated charge (Fig. 3g) as the system returns to its pre-excited equilibrium state. Note that a concentration overpotential drives oxidation between 10 μs and 1 ms (i.e., the diffusion time scale) in both cases. In the cathodic case, this concentration overpotential works against the uniformly negative interfacial potential to produce net oxidation. Thus, negative charge briefly continues to accumulate at the electrode until the discharging reduction reactions are finally able to overcome the dissipating concentration overpotential at approximately 2 ms (Fig. 5b).

The preferential anodic or cathodic discharge manifests as the BPE floating to either a positive or negative potential, respectively,

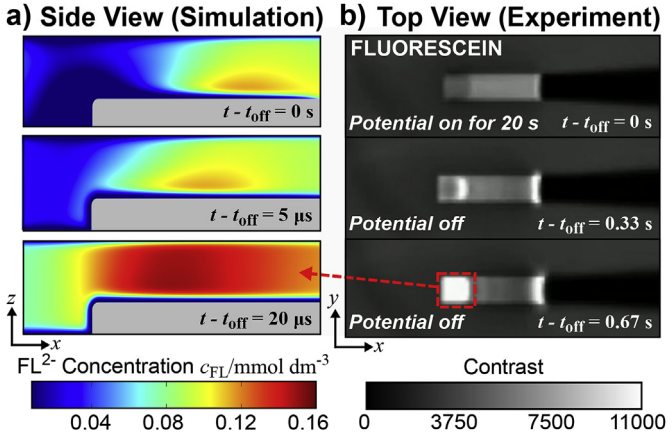

Fig. 4. (a) Simulation results and (b) experimental fluorescence intensities at various times during EDL relaxation. The top frame in (b) shows the fluorescein fluorescence intensity distribution for a nanochannel-confined BPE after 20 s of charging under an applied 250 V. After this potential is removed, fluorescein redistribution by drift-diffusion manifests as a rapid increase in concentration at the cathode due to the large influx of anions required to neutralize the cathodic EDL (positive) space charge imbalance. Simulation results in (a) are shown for a cathodic case, but this electrokinetic concentration enhancement occurs to some extent in all three cases. Note that the 10^5-fold absolute time scale difference between simulation and experiment arises due to disparities in length scales (5 µm vs. 1 cm), as well as limitations on how quickly the applied potential can be practically removed by the power supply.

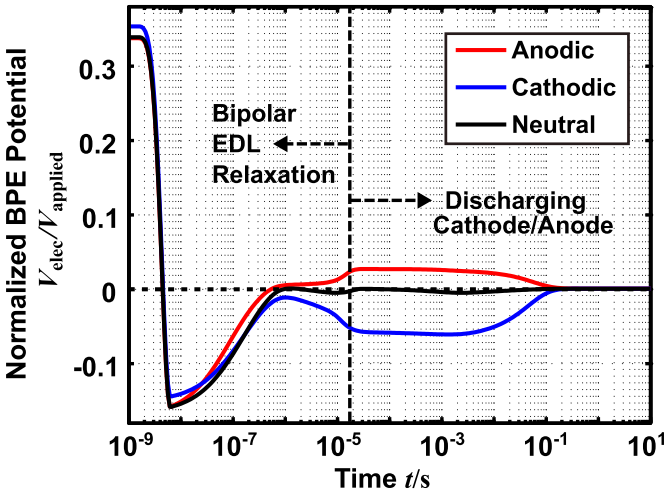

Fig. 6. Floating BPE potential during discharge. The BPE eventually floats to a positive value in the anodic case and a negative value in the cathodic case in order to shed the accumulated charge via spontaneous electrochemical reactions before returning to equilibrium.

during the Galvanic discharge period (Fig. 6, $t > \sim 10$ µs). Note that the fluid potential far away from the BPE has effectively reached zero by this point, thus reinforcing the notion that the BPE eventually acts as either a cathode or anode with a uniform driving potential of single polarity. A notable feature of the BPE floating potential response is that, for all three cases, the electrode potential in the charged state ($t = 0$ s) is considerably less than half of the applied potential. Under the leading-order simplifying assumptions of uniform solution composition and relatively slow Faradaic reaction kinetics (i.e., a small portion of the total system current passing through the BPE), the potential drop in solution is linear along the channel length and the electrode would float to half of the applied potential if the reaction kinetics at the poles were symmetric (i.e., the neutral case). As with a Galvanic cell, one would then expect any reaction asymmetry and the subsequent accumulation of positive or negative charge to shift the potential to higher or lower values, respectively. In practice, however, electric field gradients associated with CP in confined BPE systems can induce large Ohmic potential drops upstream of the cathode [37,42], resulting in the BPE being exposed to a smaller than expected end-to-end potential difference during the charging phase and subsequently floating to a lower potential than expected for all three cases. If the channel walls were positively charged, the background EOF direction would be reversed and ion depletion would instead occur near the anode, leading to a higher BPE potential than expected (Ohmic losses to the right of the BPE would still lead to a smaller end-to-end potential difference than expected, however). Therefore, the applied potentials required to initiate and sustain Faradaic reactions can be higher than predicted by theoretical approximations [43].

Redox reactions must necessarily accompany the discharging process, as interfacial charge transfer is the sole mechanism by which the net accumulated charge (or adsorbed redox species, in the case of pseudocapacitors [6]) is shed from the isolated BPE. Since the anodic case is characterized by oxidation reactions and

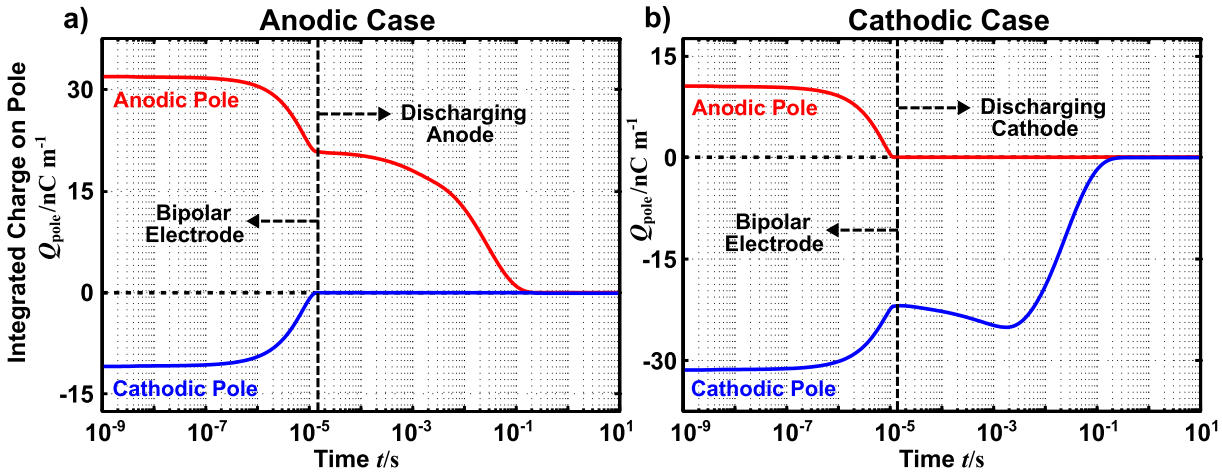

Fig. 5. Integrated charge per unit width (polarization + electrochemically accumulated charge) on the respective poles over time for the cases of (a) a net positive charge and (b) a net negative charge accumulated at the BPE. The curves were calculated by multiplying the interfacial potential distributions from Fig. 2 by the Stern layer capacitance and separately integrating the positive and negative regions at each time. Results for both cases suggest that for the simulated conditions, the BPE loses its polarization around 10 µs and shortly thereafter transitions to become a spontaneously discharging anode or cathode.

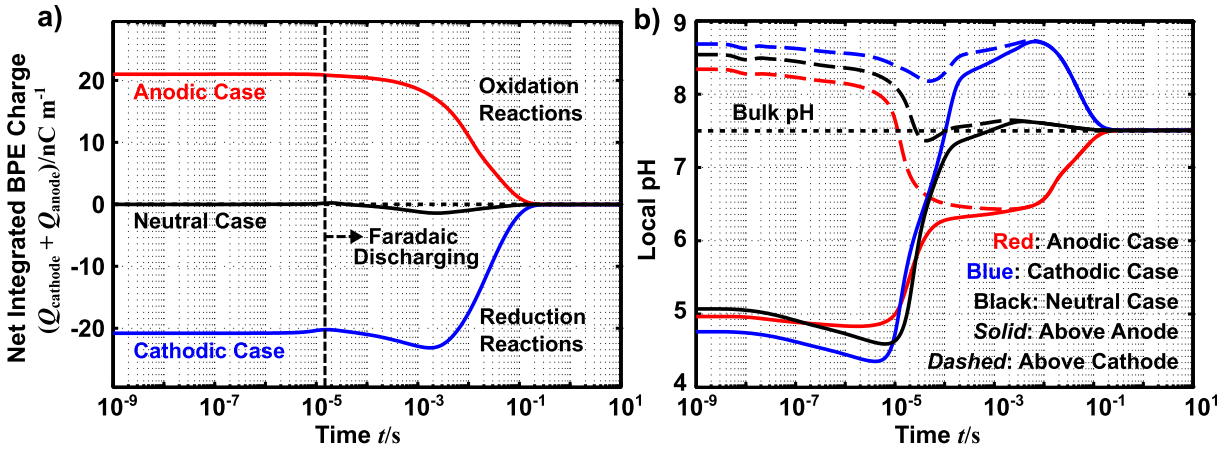

Fig. 7. Discharging reactions: (a) Net electrochemically accumulated BPE charge per unit width present during discharge, and (b) local pH outside the EDL near both the cathode and anode for all three cases. These results indicate that there can be significant oxidation (anodic case) or reduction (cathodic case) reactions that must take place for the BPE to fully discharge; these reactions are accompanied by the production of H^+ or OH^- ions, respectively, and subsequently influence the local pH near the electrode poles.

the cathodic case is characterized by reduction reactions which drive the Faradaic discharge process (Fig. 7a), the electrokinetics and chemical reactions associated with the redox-active ions produced by these discharging reactions will be qualitatively different for the two cases. That is, the oxidation reactions in the anodic case will produce O_2 and H^+ (resulting in a drop in the local pH) and the reduction reactions in the cathodic case will produce H_2 and OH^- (resulting in a local pH rise). A similar effect has been previously reported [11] and leveraged for pseudocapacitive analyte detection using conventional (non-bipolar) electrodes with adsorbed redox species; the potential advantages of such detection schemes coupled to "wireless" bipolar electrochemistry are promising and merit further investigation. The electrochemically-driven pH changes in our simulation start to occur rapidly at ~10 μs (Fig. 7b), corresponding to the time at which the BPE transitions to a spontaneous Galvanic discharge-dominated regime (Ohmic time). As suggested by Fig. 7b, these discharging reactions and the associated pH changes should occur uniformly above the electrode, such that the entire spatial region near the BPE eventually becomes acidic for the anodic case, alkaline for the cathodic case, and near the bulk pH for the neutral case. However, we will show in the next section that this expectation is not in accordance with experimental observations, as electrochemical modification of the surface under a polarizing field noticeably affects the discharging dynamics.

4.2. Effect of BPE oxide growth

The numerical results from the preceding sections have neglected the formation and presence of surface oxides on the bipolar electrode. In practice, however, platinum anodes are known to be susceptible to oxidation after sustained reactions [58]. We can qualitatively account for the effects of surface oxide film formation on the electrokinetic and electrochemical dynamics of our system by approximating some portion of the oxygen evolution current density as contributing to the formation and growth of platinum oxide on the surface. That is, we make the simplifying assumption that the oxide growth rate is proportional to the local oxidation current from the OER and neglect the current contribution arising from the oxide growth (i.e., we assume an OER-dominant regime [59]),

$$\frac{\partial h_{\text{film}}}{\partial t} = \varphi j_{\text{F,O}_2}, \tag{12}$$

where h_{film} is the local film thickness, and ϕ is a proportionality constant that relates the rate of charge transfer to that of the oxide growth (Fig. 8a). We assume arbitrary values ranging from 1×10^{-14} m^3/C to 3×10^{-13} m^3/C for the proportionality constant, as we only anticipate a qualitative representation from our model. A characteristic time scale for the growth of 1 nm of oxide can be estimated from $\tau_{\text{og,nm}} = (1\ \text{nm})\left(\varphi j_{0,\text{O}_2}\right)^{-1}$, which yields $\tau_{\text{og,nm}} = 100$ s for $\phi = 2 \times 10^{-13}$ m^3/C in our model.

The oxide film accordingly develops and grows thickest at the extremity of the anodic pole (Fig. 8b), while the thickness is equal to zero for the entire cathodic pole. This film acts as a resistive layer which serves to decrease the local interfacial potential difference between the BPE and the diffuse layer of the electrolyte solution. Thus, the interfacial potential difference now includes an additional Ohmic potential drop across the film $V_{\text{film}} = j_{\text{F,net}} R_{\text{film}}$, where R_{film} is the surface film resistance, given by $R_{\text{film}} = h_{\text{film}}/\kappa_{\text{film}}$ (for the purposes of this qualitative simulation we assume the conductivity of the film κ_{film} to be equal to 1×10^{-6} S/m). The local interfacial potential difference that drives Faradaic reactions now changes from $V_{\text{elec}} - \psi$ to $V_{\text{elec}} - \psi - V_{\text{film}}$. Note that the film thickness, and thus the Ohmic potential drop, are fixed to zero in locations where no net oxidation has occurred (the film thickness cannot numerically become negative at the cathodic pole).

The reactions at the cathodic and anodic poles of the electrode are inherently coupled, much like those of a working and counter electrode in a conventional electrochemical system. Therefore, as oxide growth hinders the reactions at the anodic pole, the cathodic reactions must slow due to the increased resistance in the electrochemical circuit. This effect manifests as a shift in the BPE floating potential to higher values over time, which decreases the magnitude of the interfacial potential difference at the cathode and thereby counteracts the oxide-resistance-induced decrease in the anodic interfacial potential. Thus, the total Faradaic current passing through the BPE decreases over time due to the concomitant decrease in driving potential at the two poles (Fig. 8c). As a consequence of this surface passivation, it is unlikely that a true steady state is ever achieved in a reasonable experimental timeframe using an oxide-forming conductive BPE material such as Pt.

As previously alluded to, the presence of a resistive film on the

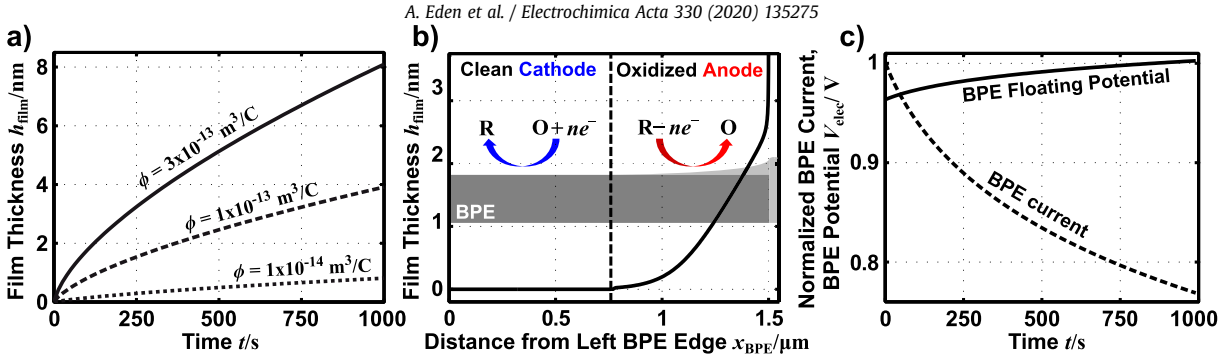

Fig. 8. Influence of oxide growth: (a) Simulation of oxide film growth at the anodic pole under an applied field, (b) local oxide profile along the BPE surface after 1000 s of reactions, and (c) shift in the BPE floating potential towards the cathodic pole to compensate for the resistive oxide film growth; this shift serves to reduce the cathodic interfacial potential in order to balance currents and conserve charge, and the net current passing through the BPE subsequently decreases over time. Profiles in (b) and (c) are shown for $\phi = 1 \times 10^{-13}$ m^3/C.

BPE surface also noticeably affects the experimentally observed discharging dynamics and the coupled chemical and electrokinetic events which accompany discharging. In particular, the observed sequence of events suggests that, contrary to the results predicted in Fig. 7, the pH does not drop uniformly around the BPE during discharge for an anodic case. Instead, shortly after the fluorescence intensity rise associated with anionic influx at the cathodic pole during the Ohmic time, rapid and intense fluorescence quenching linked to water oxidation products was seen to affect the pH-sensitive FL dye locally above the left pole only (Fig. 9). This localization can be attributed to the presence of a thick oxide film, which hinders discharging reactions at the oxide-laden right pole and causes the Galvanic discharge to occur more rapidly at the left pole due to its lower interfacial resistance [41].

The influence of the surface oxide was probed experimentally in our previous work [41] by utilizing a split BPE configuration [40,60], which allowed for the two poles to be individually addressed and electrochemically pretreated separately. Briefly, the oxidation pretreatment consisted of holding the left pole at 1.2 V for 30 s to render the surface composition more uniform as the right pole became oxidized during subsequent experiments. In a separate experiment, the left pole was pre-reduced by applying −0.6 V for 10 s to remove any native oxide on the surface and amplify the effects of the subsequent nonuniform surface composition. The two split poles were then electrically connected to each other, allowing the continuous conductor to function as a floating BPE once an electric field was introduced in solution. Fig. 9 shows that the pre-oxidized BPE prevents localized discharging-linked fluorescence quenching from occurring in the same manner, intensity, and time-scale as observed with an untreated (Fig. 9a) or pre-reduced (Fig. 9b) BPE. These results confirm that the presence of the thick anodic oxide film plays an important role in influencing local discharging rates, as well as homogeneous chemical reactions and electrokinetic dynamics; the ability to understand, model, and exploit these dynamics has profound implications for the rapidly expanding domain of bipolar electrochemistry as an analytical tool for multiplexed optical and electrical screening/detection of molecules.

5. Conclusion

In this work, we numerically and experimentally explored the discharging dynamics of a nanochannel-confined BPE. The comprehensive 2D numerical model employed herein explicitly resolves diffuse-charge screening and incorporates nonlinear surface capacitance effects of the compact Stern layer, enabling us to simultaneously capture the phenomena of BPE EDL charging/relaxation (EDL capacitance) and Faradaic charge accumulation/discharge, as well as the inherent coupling of these events to solution-phase reactions and transport processes that manifest across disparate time scales. Our results suggest that, in general, three different charged BPE states are possible: (1) an anodic case in which a net positive excess charge accumulates at the BPE surface, (2) a cathodic case in which a net negative charge accumulates, and (3) a neutral case with little to no net charge accumulation; these conditions are fundamentally linked to the symmetry of the

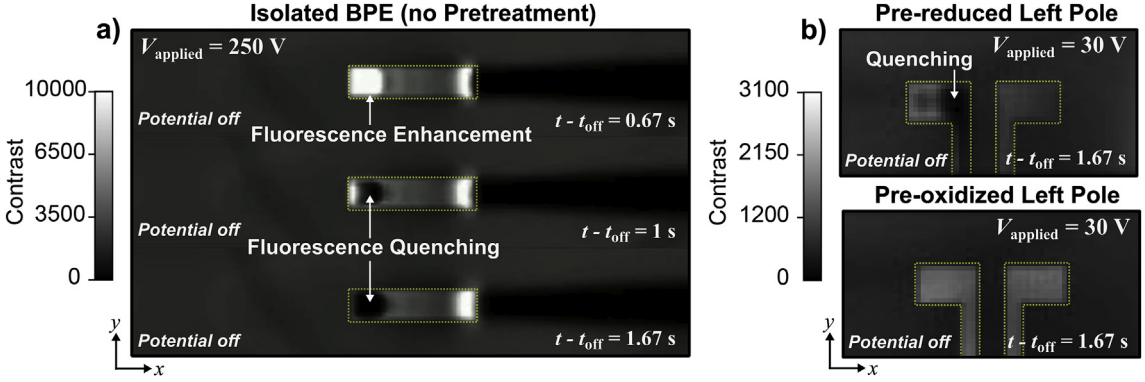

Fig. 9. Depiction of localized fluorescence quenching at the left pole of the BPE (outlined in yellow) associated with water oxidation products during anodic discharge: (a) the presence of the anodic oxide film increases the local interfacial resistance, causing the discharge to preferentially occur at the left pole, and (b) pre-oxidation of the left pole in a split BPE configuration suppresses the localized quenching effect. Note that any fluorescence quenching in the right half of the images is a result of oxidation that occurred under the applied potential. (For interpretation of the references to color in this figure legend, the reader is referred to the Web version of this article.)

forward and reverse cell reactions at the poles in a manner reminiscent of spontaneous Galvanic cells, and the resulting surface charging effects manifest as a bias in the interfacial charge/potential distribution along the BPE surface.

We were able to numerically reproduce experimentally-visualized transient enrichment of charged fluorophores, which occurred due to capacitive discharging of the bipolar EDL space charge upon abrupt removal of the driving electric field. Moreover, we showed that these dissipating nanoscale EDLs maintain an intrinsic electrostatic potential and subsequently continue to polarize the BPE until relaxation occurs on a characteristic RC time scale dictated by the EDL capacitance and solution resistance. Upon EDL relaxation, electrochemically accumulated charge causes the electrode (which is no longer bipolar) to float to a nonequilibrium potential as the excess charge is electrochemically discharged by either water oxidation (anodic case) or reduction (cathodic case). These discharging redox reactions are invariably accompanied by local perturbations in the solution composition surrounding the BPE, an effect which can ostensibly be tuned and leveraged for parallelized molecular detection; for example, the products of water oxidation were indirectly observed through fluorescence quenching of fluorescein as the BPE discharged after exposure to a sufficiently large polarizing field. The discharge rate proved to be a strong function of the electrode surface conditions; it was observed that a thick oxide layer formed at the anodic pole locally hindered discharging reactions and led the Faradaic discharge to occur predominantly at the opposite end of the BPE. Finally, we qualitatively investigated the influence of such a passivating surface oxide in our numerical model and demonstrated a gradual shift towards higher BPE floating potential values over time as the system compensated for the increasing potential drop across a growing anodic oxide film.

Our numerical model and the results presented in this work provide important insight into the coupled nanoscale electrokinetic and electrochemical phenomena that govern BPE charging and discharging processes. Importantly, the modeling approach and findings described herein are not just relevant within the field of bipolar electrochemistry, but are more broadly applicable to the wide range of electrochemical systems which exploit electrochemical transients and/or are fundamentally impacted by surface oxidation. We therefore believe that the incorporation and further extension of our comprehensive multiscale model in future electrochemical engineering efforts could yield novel approaches and transformative avenues of research within the burgeoning domain of micro- and nanoelectrochemistry.

Declaration of competing interest

None.

Acknowledgements

This work was supported by the Institute for Collaborative Biotechnologies through grants (W911NF-09-001 and DAAD19-03-D-0004) from the U.S. Army Research Office. The content of the information does not necessarily reflect the position or the policy of the Government, and no official endorsement should be inferred.

Appendix A. Supplementary data

Supplementary data to this article can be found online at https://doi.org/10.1016/j.electacta.2019.135275.

References

[1] J.B. Goodenough, K.-S. Park, The Li-ion rechargeable battery: a perspective, J. Am. Chem. Soc. 135 (2013) 1167–1176, https://doi.org/10.1021/ja3091438.
[2] R. O'Hayre, S.-W. Cha, W.G. Colella, F.B. Prinz, Fuel Cell Fundamentals, Prentice-Hall, Inc., New Jersey, 2016, https://doi.org/10.1002/9781119191766.
[3] S. Litster, G. McLean, PEM fuel cell electrodes, J. Power Sources 130 (2004) 61–76, https://doi.org/10.1016/j.jpowsour.2003.12.055.
[4] P. Alotto, M. Guarnieri, F. Moro, Redox flow batteries for the storage of renewable energy: a review, Renew. Sustain. Energy Rev. 29 (2014) 325–335, https://doi.org/10.1016/j.rser.2013.08.001.
[5] B.E. Conway, Electrochemical Supercapacitors: Scientific Fundamentals and Technological Applications, Springer, Boston, 1999, https://doi.org/10.1007/978-1-4757-3058-6.
[6] D.P. Dubal, O. Ayyad, V. Ruiz, P. Gómez-Romero, Hybrid energy storage: the merging of battery and supercapacitor chemistries, Chem. Soc. Rev. 44 (2015) 1777–1790, https://doi.org/10.1039/C4CS00266K.
[7] R.S. Nicholson, Theory and application of cyclic voltammetry for measurement of electrode reaction kinetics, Anal. Chem. 37 (1965) 1351–1355, https://doi.org/10.1021/ac60230a016.
[8] E. Laviron, The use of linear potential sweep voltammetry and of a.c. voltammetry for the study of surface electrochemical reaction of strongly adsorbed systems and of redox modified electrodes, J. Electroanal. Chem. Interfacial Electrochem. 100 (1979) 263–270, https://doi.org/10.1016/S0022-0728(79)80167-9.
[9] F. Mansfield, Use of electrochemical impedance spectroscopy for the study of corrosion protection by polymer coatings, J. Appl. Electrochem. 25 (1995) 187–202, https://doi.org/10.1007/BF00262955.
[10] H.-K. Song, Y.-H. Jung, K.-H. Lee, L.H. Dao, Electrochemical impedance spectroscopy of porous electrodes: the effect of pore size distribution, Electrochim. Acta 44 (1999) 3513–3519, https://doi.org/10.1016/S0013-4686(99)00121-8.
[11] J.T.C. Barragan, E.T.S.G. da Silva, A.C.M. de Moraes, L.T. Kubota, A novel approach for electroanalytical determinations employing discharge of pseudocapacitor by electroactive species, Anal. Chim. Acta 1006 (2018) 1–9, https://doi.org/10.1016/j.aca.2017.12.024.
[12] E. Morales-Narváez, L. Baptista-Pires, A. Zamora-Gálvez, A. Merkoçi, Graphene-based biosensors: going simple, Adv. Mater. 29 (2017) 1604905, https://doi.org/10.1002/adma.201604905.
[13] M.F. El-Kady, R.B. Kaner, Scalable fabrication of high-power graphene micro-supercapacitors for flexible and on-chip energy storage, Nature Comms 4 (2013) 1475, https://doi.org/10.1038/ncomms2446.
[14] D. Erickson, D. Sinton, D. Psaltis, Optofluidics for energy applications, Nat. Photonics 5 (2011) 583–590, https://doi.org/10.1038/nphoton.2011.209.
[15] R. Gao, Y.-L. Ying, Y.-X. Hu, Y.-J. Li, Y.-T. Long, Wireless bipolar nanopore electrode for single small molecule detection, Anal. Chem. 89 (2017) 7382–7387, https://doi.org/10.1021/acs.analchem.7b00729.
[16] W. Xu, K. Fu, P.W. Bohn, Electrochromic sensor for multiplex detection of metabolites enabled by closed bipolar electrode coupling, ACS Sens. 2 (2017) 1020–1026, https://doi.org/10.1021/acssensors.7b00292.
[17] K. Dawson, A. Wahl, S. Barry, C. Barrett, N. Sassiat, A.J. Quinn, A. O'Riordan, Fully integrated on-chip nano-electrochemical devices for electroanalytical applications, Electrochim. Acta 115 (2014) 239–246, https://doi.org/10.1016/j.electacta.2013.10.144.
[18] M.Z. Bazant, K.T. Chu, B.J. Bayly, Current-voltage relations for electrochemical thin films, SIAM J. Appl. Math. 65 (2005) 1463–1484, https://doi.org/10.1137/040609938.
[19] H. Wang, L. Pilon, Accurate simulations of electric double layer capacitance of ultramicroelectrodes, J. Phys. Chem. C 115 (2011) 16711–16719, https://doi.org/10.1021/jp204498e.
[20] G.M. Whitesides, A.D. Stroock, Flexible methods for microfluidics, Phys. Today 54 (2001) 42–48, https://doi.org/10.1063/1.1387591.
[21] A. Frumkin, Hydrogen overpotential and the double layer structure, Z. Phys. Chem. 164 (1933) 121–133, https://doi.org/10.1515/zpch-1933-16411.
[22] A. Bonnefont, F. Argoul, M.Z. Bazant, Analysis of diffuse-layer effects on time-dependent interfacial kinetics, J. Electroanal. Chem. 500 (2001) 52–61, https://doi.org/10.1016/S0022-0728(00)00470-8.
[23] M.Z. Bazant, K. Thornton, A. Ajdari, Diffuse-charge dynamics in electrochemical systems, Phys. Rev. E. 70 (2004), 021506, https://doi.org/10.1103/PhysRevE.70.021506.
[24] M. van Soestbergen, Frumkin-Butler-Volmer theory and mass transfer in electrochemical cells, Russ. J. Electrochem. 48 (2012) 570–579, https://doi.org/10.1134/S1023193512060110.
[25] P.M. Biesheuvel, M. van Soestbergen, M.Z. Bazant, Imposed currents in galvanic cells, Electrochim. Acta 54 (2009) 4857–4871, https://doi.org/10.1016/j.electacta.2009.03.073.
[26] M. van Soestbergen, Diffuse layer effects on the current in galvanic cells containing supporting electrolyte, Electrochim. Acta 55 (2010) 1848–1854, https://doi.org/10.1016/j.electacta.2009.10.078.
[27] M. van Soestbergen, P.M. Biesheuvel, M.Z. Bazant, Diffuse-charge effects on the transient response of electrochemical cells, Phys. Rev. E 81 (2010), 021503, https://doi.org/10.1103/PhysRevE.81.021503.
[28] M. Rossi, T. Wallmersperger, S. Neukamm, K. Padberg-Gehle, Modeling and simulation of electrochemical cells under applied voltage, Electrochim. Acta 258 (2017) 241–254, https://doi.org/10.1016/j.electacta.2017.10.047.

[29] Y.-L. Ying, Y.-X. Hu, R. Gao, R.-J. Yu, Z. Gu, L.P. Lee, Y.-T. Long, Asymmetric nanopore electrode-based amplification for electron transfer imaging in live cells, J. Am. Chem. Soc. 140 (2018) 5385–5392, https://doi.org/10.1021/jacs.7b12106.
[30] J. Duval, J.M. Kleijn, H.P. van Leeuwen, Bipolar electrode behavior of the aluminum surface in a lateral electric field, J. Electroanal. Chem. 505 (2001) 1–11, https://doi.org/10.1016/S0022-0728(01)00461-2.
[31] W. Wei, G. Xue, E.S. Yeung, One-step concentration of analytes based on dynamic change in pH in capillary zone electrophoresis, Anal. Chem. 74 (2002) 934–940, https://doi.org/10.1021/ac015617t.
[32] R.K. Anand, E. Sheridan, K.N. Knust, R.M. Crooks, Bipolar electrode focusing: faradaic ion concentration polarization, Anal. Chem. 83 (2011) 2351–2358, https://doi.org/10.1021/ac103302j.
[33] D.R. Laws, D. Hlushkou, R.K. Perdue, U. Tallarek, R.M. Crooks, Bipolar electrode focusing: simultaneous concentration enrichment and separation in a microfluidic channel containing a bipolar electrode, Anal. Chem. 81 (2009) 8923–8929, https://doi.org/10.1021/ac901545y.
[34] C. Ulrich, O. Andersson, L. Nyholm, F. Björefors, Formation of molecular gradients on bipolar electrodes, Angew. Chem. 120 (2008) 3076–3078, https://doi.org/10.1002/ange.200705824.
[35] S.E. Fosdick, R.M. Crooks, Bipolar electrodes for rapid screening of electrocatalysts, J. Am. Chem. Soc. 134 (2012) 863–866, https://doi.org/10.1021/ja210354m.
[36] S.E. Fosdick, K.N. Knust, K. Scida, R.M. Crooks, Bipolar electrochemistry, Angew. Chem. Int. Ed. 52 (2013) 10438–10456, https://doi.org/10.1002/anie.201300947.
[37] R. Dhopeshwarkar, D. Hlushkou, M. Nguyen, U. Tallarek, R.M. Crooks, Electrokinetics in microfluidic channels containing a floating electrode, J. Am. Chem. Soc. 130 (2008) 10480–10481, https://doi.org/10.1021/ja8036405.
[38] G.M. Crouch, D. Han, S.K. Fullerton-Shirey, D.B. Go, P.W. Bohn, Addressable direct-write nanoscale filament formation and dissolution by nanoparticle-mediated bipolar electrochemistry, ACS Nano 11 (2017) 4976–4984, https://doi.org/10.1021/acsnano.7b01657.
[39] T.M. Braun, D.T. Schwartz, Bipolar electrochemical displacement: a new phenomenon with implications for self-limiting materials patterning, ChemElectroChem 3 (2016) 441–449, https://doi.org/10.1002/celc.201500356.
[40] O. Ordeig, N. Godino, J. del Campo, F.X. Muñoz, F. Nikolajeff, L. Nyholm, On-chip electric field driven electrochemical detection using a poly(-dimethylsiloxane) microchannel with gold microband electrodes, Anal. Chem. 80 (2008) 3622–3632, https://doi.org/10.1021/ac702570p.
[41] K. Scida, A. Eden, N. Arroyo-Currás, S. MacKenzie, Y. Satik, C.D. Meinhart, J.C.T. Eijkel, S. Pennathur, Fluorescence-based observation of transient electrochemical and electrokinetic effects at nanoconfined bipolar electrodes, ACS Appl. Mater. Interfaces 11 (2019) 13777–13786, https://doi.org/10.1021/acsami.9b01339.
[42] A. Eden, K. Scida, N. Arroyo-Currás, J.C.T. Eijkel, C.D. Meinhart, S. Pennathur, Modeling Faradaic reactions and electrokinetic phenomena at a nanochannel-confined bipolar electrode, J. Phys. Chem. C 123 (2019) 5353–5364, https://doi.org/10.1021/acs.jpcc.8b10473.
[43] T.M. Squires, M.Z. Bazant, Induced-charge electro-osmosis, J. Fluid Mech. 509 (2004) 217–252, https://doi.org/10.1017/s0022112004009309.
[44] A. Mani, T.A. Zangle, J.G. Santiago, On the propagation of concentration polarization from microchannel-nanochannel interfaces part I: analytical model and characteristic analysis, Langmuir 25 (2009) 3898–3908, https://doi.org/10.1021/la803317p.
[45] A. Eden, C. McCallum, B.D. Storey, S. Pennathur, C.D. Meinhart, Analyte preconcentration in nanofluidic channels with nonuniform zeta potential, Phys. Rev. Fluids 2 (2017) 124203, https://doi.org/10.1103/PhysRevFluids.2.124203.
[46] W. Liu, Y. Ren, F. Chen, J. Song, Y. Tao, K. Du, Q. Wu, A microscopic physical description of electrothermal-induced flow for control of ion current transport in microfluidics interfacing nanofluidics, Electrophoresis 40 (2019) 2683–2698, https://doi.org/10.1002/elps.201900105.
[47] K.J. Vetter, Electrochemical Kinetics: Theoretical and Experimental Aspects, Academic Press, Inc., New York, 1967.
[48] L. Bouffier, T. Doneux, B. Goudeau, A. Kuhn, Imaging redox activity at bipolar electrodes by indirect fluorescence modulation, Anal. Chem. 86 (2014) 3708–3711, https://doi.org/10.1021/ac500623v.
[49] T. Teorell, Transport processes and electrical phenomena in ionic membranes, Prog. Biophys. Biophys. Chem. 3 (1953) 305–369, https://doi.org/10.1016/S0096-4174(18)30049-0.
[50] A. Bard, L. Faulkner, Electrochemical Methods: Fundamentals and Applications, John Wiley & Sons, New York, 2001.
[51] S.H. Behrens, D.G. Grier, The charge of glass and silica surfaces, J. Chem. Phys. 115 (2001) 6716–6721, https://doi.org/10.1063/1.1404988.
[52] F. Booth, Dielectric constant of polar liquids at high field strengths, J. Chem. Phys. 23 (1955) 453–457, https://doi.org/10.1063/1.1742009.
[53] O. Stern, The theory of the electrolytic double layer, Z. Elektrochem. Angew. Phys. Chem. 30 (1924) 508–516.
[54] L.H. Olesen, H. Bruus, A. Ajdari, Ac electrokinetic micropumps: the effect of geometrical confinement, faradaic current injection, and nonlinear surface capacitance, Phys. Rev. E 73 (2006), 056313, https://doi.org/10.1103/physreve.73.056313.
[55] C.C.M. Groot, H.J. Bakker, A femtosecond mid-infrared study of the dynamics of water in aqueous sugar solutions, Phys. Chem. Chem. Phys. 17 (2015) 8449–8458, https://doi.org/10.1039/c4cp05431h.
[56] F. Haber, R. Russ, Über die elektrische reduction, Z. Phys. Chem. 47 (1904) 257–335, https://doi.org/10.1515/zpch-1904-4722.
[57] S.S. Dukhin, Electrokinetic phenomena of the 2nd kind and their applications, Adv. Colloid Interface Sci. 35 (1991) 173–196, https://doi.org/10.1016/0001-8686(91)80022-c.
[58] F.P. Bowden, The amount of hydrogen and oxygen present on the surface of a metallic electrode, Proc. R. Soc. London, Ser. A 125 (1929) 446–462, https://doi.org/10.1098/rspa.1929.0178.
[59] V.I. Birss, A. Damjanovic, P.G. Hudson, Oxygen evolution at platinum electrodes in alkaline solutions II. mechanism of the reaction, J. Electrochem. Soc. 133 (1986) 1621–1625, https://doi.org/10.1149/1.2108978.
[60] K.-F. Chow, F. Mavré, J.A. Crooks, B.-Y. Chang, R.M. Crooks, A large-scale, wireless electrochemical bipolar electrode microarray, J. Am. Chem. Soc. 131 (2009) 8364–8365, https://doi.org/10.1021/ja902683f.